PNAS

Measuring prion propagation in single bacteria elucidates a mechanism of loss

Krista Jager[a,1], Maria Teresa Orozco-Hidalgo[a,1] (iD), Benjamin Lennart Springstein[b] (iD), Euan Joly-Smith[c] (iD), Fotini Papazotos[a], EmilyKate McDonough[b] (iD), Eleanor Fleming[b] (iD), Giselle McCallum[a] (iD), Andy H. Yuan[d], Andreas Hilfinger[c,e,f] (iD), Ann Hochschild[b,2] (iD), and Laurent Potvin-Trottier[a,g,h,2] (iD)

Prions are self-propagating protein aggregates formed by specific proteins that can adopt alternative folds. Prions were discovered as the cause of the fatal transmissible spongiform encephalopathies in mammals, but prions can also constitute nontoxic protein-based elements of inheritance in fungi and other species. Prion propagation has recently been shown to occur in bacteria for more than a hundred cell divisions, yet a fraction of cells in these lineages lost the prion through an unknown mechanism. Here, we investigate prion propagation in single bacterial cells as they divide using microfluidics and fluorescence microscopy. We show that the propagation occurs in two distinct modes. In a fraction of the population, cells had multiple small visible aggregates and lost the prion through random partitioning of aggregates to one of the two daughter cells at division. In the other subpopulation, cells had a stable large aggregate localized to the pole; upon division the mother cell retained this polar aggregate and a daughter cell was generated that contained small aggregates. Extending our findings to prion domains from two orthologous proteins, we observe similar propagation and loss properties. Our findings also provide support for the suggestion that bacterial prions can form more than one self-propagating state. We implement a stochastic version of the molecular model of prion propagation from yeast and mammals that recapitulates all the observed single-cell properties. This model highlights challenges for prion propagation that are unique to prokaryotes and illustrates the conservation of fundamental characteristics of prion propagation.

prions | protein-based heredity | single-cell microscopy | microfluidics | *Escherichia coli*

Prion-forming proteins (hereafter prion proteins) are proteins that can adopt multiple conformations, of which at least one is self-propagating. Prions were originally discovered as the cause of devastating neurodegenerative diseases, such as Creutzfeldt–Jakob's disease (CJD), in mammals (1). Subsequently, nonpathogenic prions were found across diverse species—such as budding yeast (2–6), *Drosophila* (7), *Arabidopsis* (8), and mammals (9–11)—where they are thought to function as protein-based carriers of epigenetic information. In many cases, the prion capability is conferred on the protein by a modular prion domain (PrD), necessary and sufficient for formation of the prion. Conversion from the soluble form to the prion form (a highly structured aggregated form in many well-studied cases) bestows a loss-of-function (12) or gain-of-function (10, 13, 14) to the attached protein, which can result in a fitness advantage under certain environmental conditions (4–6, 15, 16). A particular property of prions is that they can sometimes adopt multiple structures, called strains, each of which propagates itself with different properties. In mammals, different strains of the prion protein (PrP) are the cause of different diseases (17, 18), while in yeast different prion strains can have different properties that can result in different phenotypes (19–22). For example, strains of the intensively studied prion $[PSI^+]$ (formed by the essential translation release factor Sup35) differ in their stabilities and aggregate size distributions (19–21). In a second example, different strains of the yeast prion $[SMAUG^+]$ have been identified that produce very different phenotypes (22).

While the detailed molecular mechanisms of prion propagation are under investigation (23, 24), studies in yeast and mammals appear to be consistent with the nucleated polymerization model (25–27). In this model, proteins are converted from the soluble form to the prion form by elongation of existing oligomeric prion aggregates, while aggregates can be fragmented into smaller oligomers presumably by chaperones like Hsp104, an ATP-dependent disaggregase that is required for the propagation of $[PSI^+]$ and other prions in yeast (28). Initial conversion to the prion form is suggested to happen by the rare spontaneous oligomerization to a critical size n_c, below which oligomers would revert to the soluble form.

Significance

Prions are self-propagating protein aggregates that cause neurodegenerative diseases in mammals. In other organisms such as yeast, prions can function as nonpathogenic protein-based elements of inheritance, conferring new phenotypes that are maintained over many generations. Prions were recently discovered in bacteria, extending the phenomenon of protein-based inheritance to another domain of life. Here, taking advantage of a bacteria-based model, we develop an experimental system for investigating prion propagation and loss at the single-cell level. Using microfluidics, single-cell time-lapse microscopy, and mathematical modeling, we find that bacteria lose the prion through mispartitioning of the aggregates to one of the two daughter cells at division. Our findings highlight stability features of prion propagation that are unique to prokaryotes.

[1] K.J. and M.T.O.-H. contributed equally to this work.

[2] To whom correspondence may be addressed. Email: ann_hochschild@hms.harvard.edu or laurent.potvin@concordia.ca.

In the last decade, thousands of candidate prion domains (cPrDs) have been identified in bacteria using bioinformatic analyses (29, 30). So far, two of these domains were found to form self-propagating prion aggregates in *Escherichia coli*: the PrD from the Rho termination factor of *Clostridium botulinum*, which mediated prion formation in the context of a full-length Rho protein [*Cb* Rho, (30)] and the PrD from the single-stranded DNA-binding protein of *Campylobacter hominis* [*Ch* SSB, (31)]. Of note, many orthologs of these proteins also have predicted cPrDs (30). Although individual lineages could propagate the prions for more than a hundred generations, a fraction of the cells in each lineage was seen to have lost the prion at each replating round (30, 31). The mechanisms by which the prion is lost, and for how many generations individual cells propagate the prion, are unknown. In addition, it is not known whether or not the nucleated polymerization model, which is consistent with experimental findings obtained in yeast and mammalian systems, can also be used to describe prion propagation in bacteria.

In this study, we sought to address these questions by measuring prion propagation in single bacteria. Specifically, we use microfluidics and single-cell time-lapse microscopy to follow the propagation and loss of the *Ch* SSB PrD prion (hereafter the *Ch* SSB prion) in individual cell lineages. We note that microfluidics has been used previously to track the behavior of a synthetic model amyloid in *E. coli* (32). Our analysis revealed two types of prion-containing cells characterized by differences in aggregate size and exhibiting dramatic differences in loss kinetics. For the less stable subtype, we find that the loss of the prion was caused mainly by stochastic inheritance of the aggregates to only one of the two daughter cells at division (i.e., "partitioning errors"). We show that two orthologous SSB cPrDs also form self-propagating prion aggregates, and that the modes of propagation and loss closely resemble those of the *Ch* SSB prion. In addition and consistent with previous findings (31), we uncover evidence suggesting that bacterial prions, like yeast prions, can exist as phenotypically distinct strains. Using mathematical modeling, we implement a stochastic version of the nucleated polymerization model, which strikingly recapitulates all the observed single-cell properties. Moreover, this model enables us to make an experimentally testable prediction that further corroborates our finding that prion loss is caused by partitioning errors. The model also allows us to estimate the prion replication rate, which is found to be similar to that of mammalian prions. This work provides an assay for studying prion propagation in individual cells, provides insights into prion propagation and loss, and points to mechanistic commonalities among prion propagation mechanisms in diverse organisms.

Results

Experimental System to Track Prion Propagation and Loss in Single Cells.

To investigate how long individual cells propagate a prion and the mechanisms of prion loss, we developed an experimental system that enables us to track prion propagation in thousands of individual cells for many cell divisions (Fig. 1 *A–D*). For this, we used the previously constructed His6-mEYFP-*Ch* SSB-PrD (hereafter *Ch* SSB PrD) fusion protein (31) to visualize prion propagation using fluorescence microscopy. Like the Sup35 prion protein in yeast (33–35), *Ch* SSB PrD requires the presence of a preexisting prion known as [*PIN*⁺] (for [*PSI*⁺] inducibility) to access the prion conformation, but not for its maintenance (i.e., the propagation phase) (31). Several prion proteins can serve as [*PIN*⁺], including the *Saccharomyces cerevisiae* New1 protein

(31, 33, 35, 36). Therefore, following our previous experimental protocol (31), we used the New1 protein as a heterologous source of [*PIN*⁺] to trigger the initial conversion of *Ch* SSB-PrD to the prion form. Thus, we transiently expressed a New1-mScarlet-I fusion encoded on a temperature-sensitive plasmid. After inducing synthesis of the New1 fusion protein and subsequently curing the cells of the New1-encoding plasmid (verified by antibiotic sensitivity and absence of mScarlet-I signal, *SI Appendix*, Fig. S1 *A–C*), colonies containing prion-propagating cells were identified using a previously developed reporter system (31). Specifically, cells containing prion aggregates were previously shown to have elevated levels of the Hsp104 ortholog ClpB (required for the propagation of the *Ch* SSB prion), such that colonies containing these cells can be distinguished on X-gal-containing plates using a P*clpB-lacZ* reporter [Fig. 1*A*, (31)]. As expected, blue colonies displayed visible protein aggregation of the *Ch* SSB PrD (as observed by fluorescence microscopy) in a fraction of the cells, and cell extracts prepared from blue colony cultures contained characteristic SDS-stable aggregates (as observed by semidenaturing detergent agarose gel electrophoresis; SDD-AGE) (Fig. 1 *B* and *C*). In contrast, the cells in pale colonies showed diffuse fluorescence and contained no SDS-stable protein aggregates (Fig. 1 *B* and *C*). As previously observed (31), replating blue colonies gave both blue and pale colonies, while replating pale colonies resulted in only pale colonies (*SI Appendix*, Fig. S1*E*). We thus concluded that blue colonies contain a mixture of cells with self-propagating prion aggregates displaying aggregated fluorescence and cells with the protein in the soluble form exhibiting diffuse fluorescence.

For time-lapse microscopy, cells from a single colony containing prion-propagating cells were loaded into a microfluidic device (37) where cells are trapped in short trenches and the newborn cells are washed away by the constant flow of growth medium (Fig. 1*D*). Automated time-lapse microscopy and analysis enables us to track individual lineages for more than two dozen cell divisions while precisely measuring cell fluorescence, growth rate, size, and other characteristics. Using this approach, we observed that cells propagated the prion (aggregated fluorescence, Fig. 1*D*) over multiple cell divisions before irreversibly losing the prion (diffuse fluorescence, Fig. 1*D*). Even though the protein concentration was constant throughout the experiment (after reaching equilibrium of growth conditions, SI Materials and Methods, section 2.6.3.2 and *SI Appendix*, Fig. S2 *A–C*), individual lineages displayed remarkable variation in the duration of prion propagation; some cells lost the prion after a few divisions while others kept it for the whole duration of the experiment (∼30 divisions).

Prion Propagation Occurs through Two Distinct Modes.

We next sought to quantify how long individual cells could maintain the prion. For the analyses, we define the time of prion loss as the last time aggregates were detected using a spot-finding algorithm (SI Materials and Methods, section 2.6.3.3.1 and *SI Appendix*, Fig. S3 *A–C*). Counting the detectable aggregates showed that aggregates were both lost and generated until the irreversible loss event, supporting the idea that the prion is propagated during the experiment rather than being simply diluted (*SI Appendix*, Fig. S3 *D* and *E*). To measure the distribution of propagation duration, we calculated the fraction of tracked cells containing prion aggregates as a function of time (SI Materials and Methods, section 2.6.3.3.2). We observed a loss curve with two phases: an initial phase of rapid loss followed by a phase with a slower rate of loss (Fig. 1*E*). This result suggested that there could be
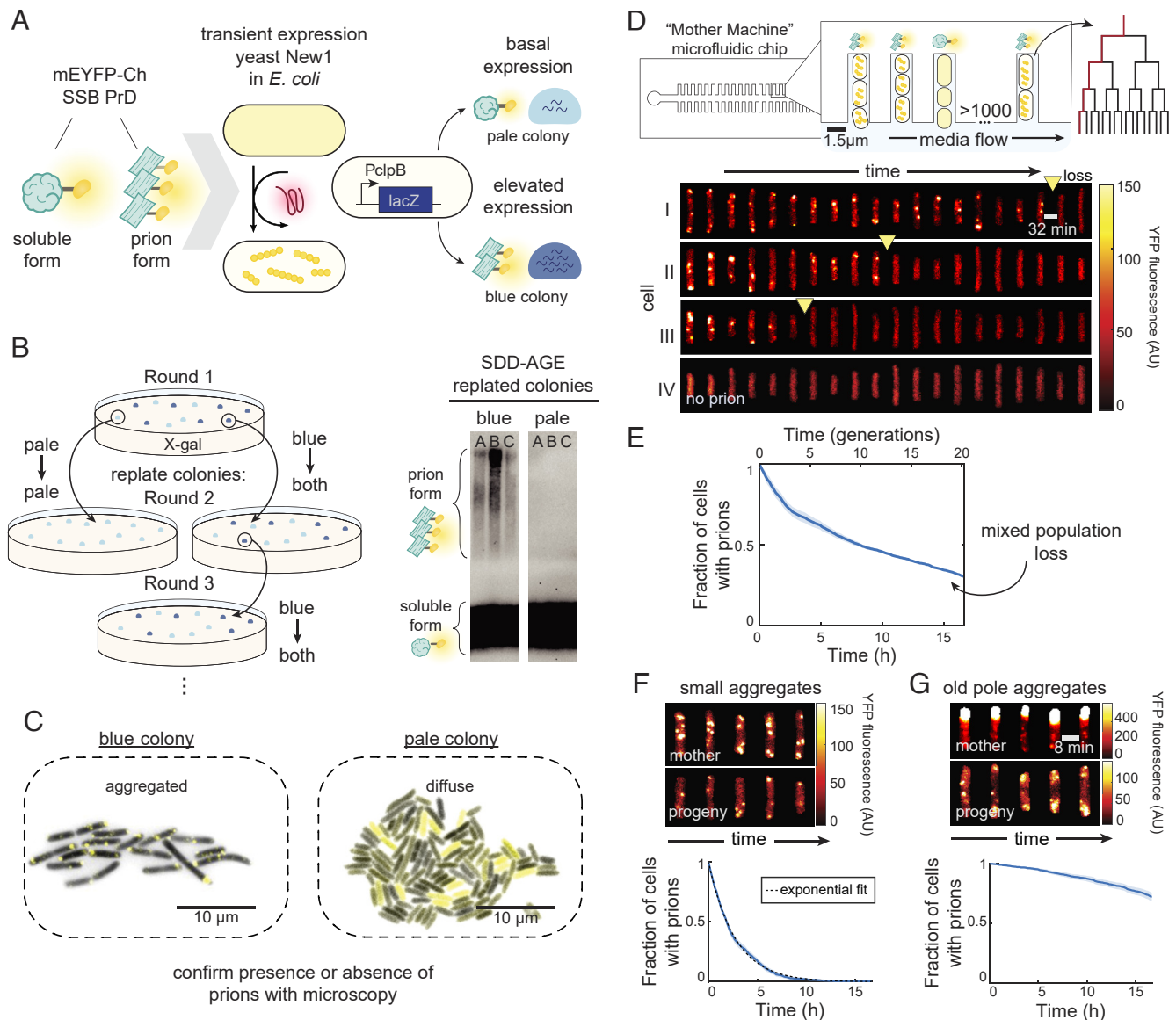
Fig. 1. Experimental setup enables quantification of prion dynamics in single cells. (*A*) Transient expression of the *S. cerevisiae* New1 protein induces conversion of His6-mEYFP-*Ch* SSB PrD from its soluble form into the prion form in *E. coli*. Bacteria with prions have elevated levels of ClpB (due presumably to the upregulation of RpoH-dependent gene expression in cells containing threshold levels of aggregated protein); thus, bacterial colonies with prion-containing cells can be distinguished from colonies with cells containing the protein in the soluble form using a P*clpB-lacZ* transcriptional reporter [blue vs pale colonies, respectively, (31)]. (*B*) Blue colonies contain self-propagating aggregates. (*Left*) Replating blue colonies results in a mix of blue and pale colonies, while replating pale colonies results in only pale colonies. (*Right*) SDD-AGE shows that different blue colony cultures (*A*, *B*, and *C*) contain SDS-stable aggregates, whereas pale colony cultures contain only soluble *Ch* SSB PrD (prion formation was induced with New1-CFP; a gel where induction was done with New1-mScarlet-I can be found in *SI Appendix*, Fig. S1D). (*C*) Fluorescence microscopy images of *E. coli* expressing His6-mEYFP-*Ch* SSB PrD shows that cells from blue colonies display visible fluorescence aggregation, whereas cells from pale colonies display diffuse YFP fluorescence. (*D*) After prion conversion, cells from a blue colony are loaded in a microfluidic device where cells are trapped in dead-end trenches, and newborn cells are washed away by the flow of growth medium. Fluorescence time-lapse microscopy montage (kymographs) of individual lineages shows that cells propagate the aggregates for heterogeneous duration (*I–III*) before irreversibly reverting to diffuse fluorescence. YFP fluorescence is shown false-colored according to the colormap indicated on the graph. The prion loss called by our spot-finding algorithm is indicated by a yellow triangle. Cells that have diffuse fluorescence at the beginning of the experiments maintain it (*IV*). (*E*) The fraction of cells with prions over time (prion loss curve) for all aggregate phenotypes shows a biphasic decay, suggesting the presence of two distinct subpopulations (*n* = 2,194 cells). (*F*) The prion loss curve for cells with small aggregates fits well to an exponential distribution (dashed line, R^2 = 0.99, *n* = 924 cells). Representative kymograph of cells with small aggregates (*Top*) (*G*) Loss curve for cells with old-pole aggregates (*n* = 2,225 cells). Kymographs for the tracked cell (mother) and its progeny (*Top*). The old-pole aggregate is mostly immobile, and the progeny contain small aggregates. The colormap for the old-pole aggregate is different as these aggregates are brighter. The standard error on the mean (SEM) in *E–G* was estimated by bootstrapping, and an envelope is shown as 2× SEM (*N* = 3 experiments for *E–G*).

two subpopulations of cells with distinct loss kinetics. Indeed, upon visual inspection of the cells, we noticed that a fraction of the cells contained a large aggregate localized to the old pole (i.e., the pole not renewed after cell division), while the rest contained multiple small and dynamic aggregates (Fig. 1 *F* and *G*). We used three different automated methods for

classifying the two types of aggregates, based on the mobility of the aggregates or the fluorescence intensity, which gave similar results (SI Materials and Methods, section 2.6.3 and *SI Appendix*, Fig. S4 *A–C*). We thus reanalyzed the loss kinetics, but this time separately for the small and old-pole aggregate types. We found that the small aggregates were lost relatively quickly, while

the old-pole aggregates were much more stable (Fig. 1 *F* and *G*). The loss curve for the small aggregates fitted well with an exponential decay with a half-life of ~1.5 h (~2 generations, Fig. 1*F*), representing a process with a constant probability of losing the prion state over time (i.e., a memoryless process). This memoryless process is consistent with previous replating experiments, where a similar fraction of prion-positive colonies is found upon successive replating (30, 31, 36). In contrast, few cells with the old-pole aggregates lost the prion over the course of the experiment, with an average loss rate of ~1 per 133 generations. The old-pole aggregates were mostly immobile, presumably because their size sterically prevents diffusion through the nucleoid (Fig. 1*G* and *SI Appendix*, Fig. S4*C*). These cells contained bona fide prion aggregates as they gave rise to progeny that contained small aggregates similar to the small and dynamic aggregates that we observed for the other cells in the device (Fig. 1*G*).

These data suggest two modes of prion propagation in *E. coli*: cells containing highly stable old-pole aggregates that give rise to a small aggregate-containing daughter cell at division and small aggregate-containing cells that lose their prion aggregates with exponential decay. In order to investigate the mechanism of

loss and model the propagation mathematically, we focused the following analyses on the cells containing small aggregates.

Prion Loss Is Mainly Driven by Partitioning Errors at Cell Division. How do cells lose the prion? A previous study in *E. coli* cells producing the yeast Sup35 PrD suggested that loss of the Sup35 prion could occur through fluctuations in the concentration of the prion protein (36). Based on previous studies in bacteria and yeast (36, 38), we hypothesized that the loss could be due to three non-mutually exclusive mechanisms: 1) stochastic variation in the concentration of the prion protein, 2) fragmentation of the aggregates below a critical size, or 3) mispartitioning of prion aggregates at cell division (Fig. 2*A*). These hypotheses lead to different predictions about the prion loss dynamics. If prion loss is caused by stochastic fluctuations in the concentration of the prion protein, the overall fluorescence intensity would be lower prior to the loss. If the loss is caused by fragmentation of the aggregates, prion loss would be uncorrelated with cell division. On the other hand, if prion loss is caused by asymmetric partitioning of aggregates, the loss would be correlated with cell division and would occur in only one of the two daughter cells.
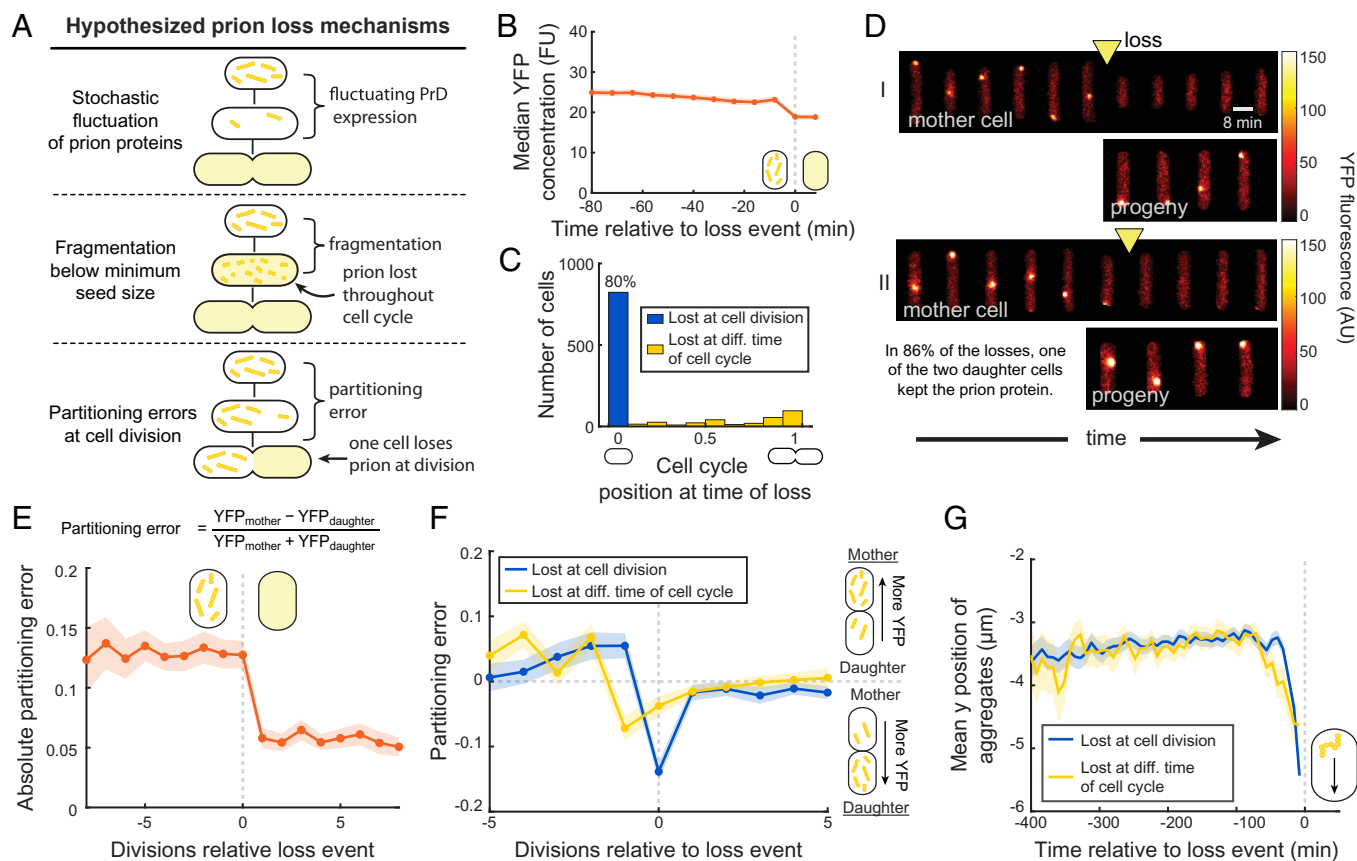

Fig. 2. Prion loss is driven by partitioning errors at cell division. (*A*) Schematic representation of the hypothesized mechanisms for prion loss in bacterial cells. (*B*) Median concentration of fluorescence (*Ch* SSB PrD) relative to the loss of the prion is constant ($n = 724$ cells). The loss event is indicated with a dotted gray line at time 0. (*C*) Histogram of the cell cycle position at the time of loss, where 0 is defined as the moment immediately after a division and 1 immediately before. Most cells (~80%) lose the prion immediately after cell division ($n = 1,117$ cells). (*D*) Kymographs of loss event show that prion loss happens in only one of the two daughter cells (86% of the losses, $n = 356$ loss events). YFP fluorescence is shown false colored according to the colormap indicated on the graph. (*E*) Mean absolute partitioning errors at the cell divisions relative to prion loss ($n = 389$ cells). The absolute partitioning error is constant prior to the loss, and higher than after the loss. (*F*) Mean partitioning errors in the cell divisions relative to the loss show that fluorescence is being transmitted to the daughter at the moment of loss for cells that lost the prion at the moment of cell division (blue lines). For the cells that lost the prion at a different moment of the cell cycle, this transfer happens one division prior to the loss (yellow line, $n = 389$ cells total). For symmetric divisions, the average partitioning error would be ~0, since molecules have an equal chance of being inherited by the mother or daughter cell. (*G*) Average longitudinal position of tracked aggregates shows that they move toward the daughter cell prior to the loss ($n = 1,117$ cells; *y* axis indicates position along the length of the cell, averaged over all detected aggregates, with the negative values indicating the distance from the top of the trench at position 0). The envelopes represent 2× SEM in *B* and *E*–*G* ($N = 3$ experiments).

By tracking prion loss in hundreds of cells with fluorescence microscopy, we could test these hypotheses. Aligning the cells at their moment of loss showed that the fluorescence was constant prior to the loss (Fig. 2B), suggesting that fluctuations in prion protein levels likely play only a minor role in the overall loss. To investigate the possibility that fragmentation of aggregates below a critical size drives the loss of the prion, we measured the position in the cell cycle at the moment of loss. We observed that ∼ 75% of cells lost the prion at the first time point after cell division (Fig. 2C). We also observed that in ∼86% of losses in the mother (the cell tracked for the duration of the experiment), the prion was maintained in the newly born daughter cell (SI Materials and Methods, section 2.6.3.4 and Fig. 2D). These observations suggested that prion loss is mainly caused by partitioning errors at cell division rather than fluctuations in prion protein levels or fragmentation of the aggregates.

Although *E. coli* divides symmetrically with proteins randomly partitioned in the daughter cells, one cell can end up with more of a particular protein by chance. These "partitioning errors"—defined as the normalized difference in the number of molecules between the daughter cells at division (Fig. 2E)—follow a binomial distribution and are generally low because on average they are inversely proportional to the square root of the number of molecules (39, 40). However, cells with the prion have relatively large aggregates, effectively reducing the number of molecules to partition. Partitioning errors at cell division were indeed on average larger and there were more frequent extreme errors (i.e., >30%) before cells lost the prion than after (Fig. 2E and *SI Appendix*, Fig. S5). In addition, the partitioning errors were constant prior to the loss (Fig. 2E), suggesting that the distribution of aggregate size was constant prior to the loss, and that this loss is a sudden rather than gradual event. This further supports the concept that the prion is being propagated until a stochastic event causes its loss. For the cells that lost the prion at cell division, fluorescent protein was found to be asymmetrically partitioned to the daughter at the moment of loss (Fig. 2F). Here, we again define the "mother" cell as the cell tracked for the duration of the experiments, and the "daughter" cells as the progeny that are eventually washed out from the device. For the cells that lost the prion at a different time during the cell cycle, a similar mispartitioning into the daughter cell was observed one division prior to the loss (Fig. 2F), suggesting that partitioning errors also play a role in the loss of the prion in these cells. Corroborating these results, tracking the position of visible aggregates revealed that they moved on average one cell length toward the daughter cell prior to both types of loss (Fig. 2G). We thus concluded that, at least in this system, prion loss is mainly caused by stochastic partitioning errors of aggregates at cell division. As we are not tracking the concentration of the disaggregase ClpB, we do not exclude the possibility that stochastic fluctuations in ClpB levels could affect the partitioning of aggregates (41), which we discuss below.

Orthologous cPrDs can Form Prions with Similar Properties. The two modes of propagation and the molecular events leading to the prion loss could be specific to the studied *Ch* SSB PrD or a more general property of bacterial prions. To begin to investigate this question, we constructed fluorescent fusions of cPrDs from SSB orthologs. We identified two orthologous SSB PrDs—from *Lactobacillus heilongjiangensis* (*Lh*) and *Moraxella lincolnii* (*Ml*, *SI Appendix*, Fig. S6A)—that could form self-propagating aggregates after transient expression of the initiation
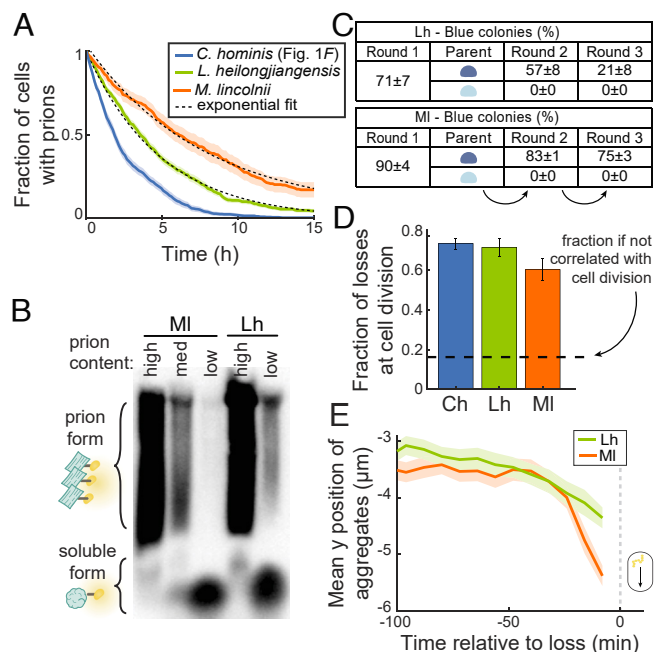

Fig. 3. Orthologous SSB cPrDs form self-propagating aggregates comparable to *Ch* SSB. (A) Prion loss curve for small aggregate cells of *Lh* SSB PrD (n = 352 cells) and *Ml* SSB PrD (n = 237 cells) compared to *Ch* SSB PrD from Fig. 1. Exponential fit curves are shown as dashed lines. (B) SDD-AGE of blue colonies confirms the presence of the aggregated prion form of *Lh* SSB and *Ml* SSB in cell extracts derived from blue colony cultures. Blue colonies with high, medium, and low prion content as estimated from fluorescence microscopy images were assayed (*SI Appendix*, Fig. S6E and section 3.1). (C) SSB orthologs form self-propagating aggregates for multiple generations. Replating blue colonies gives a mix of blue and pale colonies, while replating pale colonies results in exclusively pale colonies. (D) Fraction of prion losses at cell division shows that most losses happen at cell division for the different orthologs (n = 1,117 cells for *Ch*, 394 cells for *Lh*, 282 cells for *Ml*). The error bars represent 2× SEM as estimated by bootstrapping. The expected fraction if loss is not correlated with cell division is shown as 1/number of time points per cell cycle, representing a uniform probability of loss at all points of the cell cycle. (E) Average longitudinal position (y) of tracked aggregates shows that they move toward the daughter cell prior to the loss for the different orthologs (n = 396 cells for *Lh*, 282 cells for *Ml*). The envelopes represent 2× SEM in A and D and E (N = 3 experiments).

factor New1, as shown with fluorescence microscopy, SDD-AGE, and replating experiments (Fig. 3 A–C and *SI Appendix*, Fig. S6D). We then evaluated the properties of the aggregates formed by these PrDs in our microfluidic device. Remarkably, we found that their modes of propagation (i.e., fraction of cells with small aggregates, *SI Appendix*, Fig. S6B), loss kinetics (Fig. 3A), fraction of loss events occurring at cell division (Fig. 3D), and partitioning errors (*SI Appendix*, Fig. S6C) were similar to those formed by the *Ch* SSB PrD (though with some quantitative differences in average loss rates). Therefore, these results support the idea that the modes of prion propagation and the mechanism of prion loss through mispartitioning at cell division are not specific only to the *Ch* SSB PrD, but a more general characteristic among SSB PrDs.

A PrD can be Propagated with Distinct Kinetics in Distinct Lineages. To investigate whether or not these PrDs could form phenotypically distinguishable prion strains (19–21), we quantified prion stability in cells derived from different blue colonies representing different lineages propagating the prion. Our experimental setup provided precise and reproducible measurement of the stability; cells containing the *Lh* SSB PrD in its prion form (i.e., the *Lh* SSB prion) and obtained from
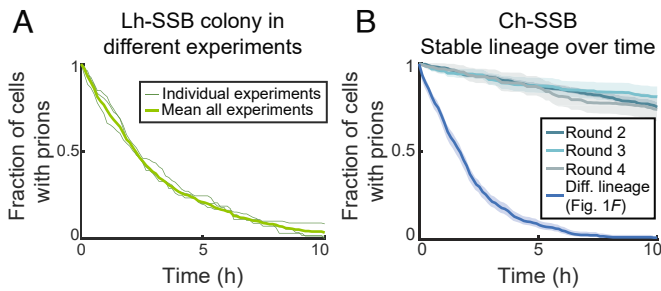
Fig. 4. Distinct bacterial lineages propagating identical prion protein exhibit distinct prion loss kinetics. (*A*) The experimental setup provides precise measurement of the prion loss kinetics. Prion loss curves for one colony of *Lh* SSB PrD in four different experiments (thin green lines, average in bold, $n = 815$ cells total). (*B*) The prion loss curve for a stable lineage of *Ch* SSB PrD remains constant over multiple rounds of growth (~37 generations each, $n = 1,018$ cells total). Round 1 refers to the first plating of induced cells cured of New1, and each subsequent round includes an overnight growth in liquid culture and plating on indicator medium. Round 2, 3, and 4 cells were obtained from a colony culture inoculated from Round 2, 3, and 4 colonies, respectively. Another lineage (from Fig. 1, dark blue line) is shown as a comparison. The envelopes represent 2× SEM as estimated by bootstrapping.

one colony exhibited similar loss kinetics during four different experiments on four different days (Fig. 4*A*). However, during our quantification of loss kinetics, we identified one lineage of cells containing the *Ch* SSB prion that exhibited unusually stable propagation. Quantifying prion stability in cells obtained from this colony in our microfluidic device revealed a loss rate an order of magnitude lower than that of the other lineages (~1 per 100 generations, Fig. 4*B*). Although the prion was much more stable, other properties such as the fraction of cells with small aggregates and the fraction of loss events occurring at the moment of cell division were similar to the other lineages (*SI Appendix*, Fig. S7 *B* and *C*). To test whether this unusual stability was self-propagating, we grew the lineage used for the microfluidic experiments for two additional rounds of about 37 generations each, loading cells from each of the successive rounds of growth into the device (Fig. 4*B*) and also replating them on indicator medium (*SI Appendix*, Fig. S7*A*). Strikingly, the loss kinetics were constant over ~110 generations and nearly all colonies were prion positive after each round of plating. DNA sequencing of the PrD-containing plasmid from cells of this lineage revealed no mutation in the promoter, the PrD, or the plasmid origin of replication (*SI Appendix*, Fig. S7*D*), suggesting that the stability property is inherited through the structure of the aggregates rather than genetically (although we could not rule out host mutations).

Physiological Impact of the Presence of Prions Aggregates. We then sought to determine the general physiological impact of such heterologous prion aggregates in *E. coli*. Among eukaryotic prions, it is striking that some are the cause of fatal neurodegenerative diseases while others appear to have low or no toxicity (1, 9–11, 17). Some studies of amyloid proteins in *E. coli* have shown a strong effect on the growth rate, e.g., a two to five-fold increase in doubling time in a well-studied case (42). In our system, a potential impact on growth rate (as a proxy for cell viability) is challenging to precisely quantify in bulk due to the different modes of prion propagation as well as the stochastic loss of the prion during growth. Thus, using our microfluidic device, we quantified the growth rate of individual cells in the absence and presence of prion aggregates. We observed that the presence of prion aggregates had an effect on the growth rate smaller than our experiment-to-experiment variability (*SI*

Appendix, Fig. S8*A*, 2× standard error of the mean (SEM) = +/− 7%). We also quantified the death rate of cells propagating the prion, and observed that the death rate was overall very low (~5 × 10^{-3}/h) and similar to cells not propagating the prion (*SI Appendix*, Fig. S8*B*). We thus concluded that the presence of prion aggregates had little impact on the overall cell physiology, at least under our experimental conditions.

A Stochastic Model Recapitulates the Experimentally Observed Prion Propagation Dynamics. Prion propagation in yeast and mammals has been mathematically modeled in various studies (19, 23–26, 43–45). We note that the nucleated polymerization model is the model for prion aggregate kinetics that is most consistent with the experimental data (19, 23–26, 44, 45). To investigate if these molecular models can describe the observed dynamics of our system, we adapted a mathematical model of prion propagation for single bacterial cells. In particular, we modeled the propagation and loss of prion aggregates in growing and dividing cells with a stochastic generalization of the nucleated polymerization model (Fig. 5*A*, details in *SI Appendix*, section 3.2). Proteins are produced in the soluble form, and can then be converted into the prion form by elongation of an existing aggregate oligomer. In the nucleated polymerization model, conversion and elongation occur in the same reaction. Aggregates can be fragmented into smaller oligomers—keeping the number of monomers constant—and aggregates below a critical size n_c spontaneously fold back into the soluble form. Cells grow continuously and divide once they reach a critical size, such that proteins are randomly partitioned between the two daughter cells according to a binomial distribution (39, 40). Individual time traces were generated using the Gillespie algorithm, which simulates the stochastic chemical reactions (48).

First, we simulated the model in a large parameter space of elongation and fragmentation rates (Fig. 5 *B* and *C*). We found that systems with large elongation and fragmentation rates were more stable as they take longer to lose the prions. Outside of this parameter space, however, the prion was eventually lost on timescales similar to our experiments. We then estimated the elongation and fragmentation rates by selecting the unique model parameters that matched the observed loss rates and partitioning errors as indicated in Fig. 5 *B* and *C* (see *SI Appendix*, section 3.2.3 for details). Strikingly, this simple model could recapitulate all the observations from the experiments. We find that simulated cells reached a quasi-stationary state, where the distribution of prion aggregates (*SI Appendix*, Fig. S9 *A–D*), the total amount of protein (Fig. 5*F*), and the absolute size of partitioning errors (Fig. 5*H*), were approximately constant prior to the loss. The quasi-stationary state prior to loss is not present in the deterministic version of the model that has been most widely studied (*SI Appendix*, section 3.2.9). Moreover, as observed experimentally, a large partitioning error into the untracked cell was observed at the moment of loss (Fig. 5*I*), which happened at cell division (Fig. 5*G*). Finally, the loss curve in the population followed an exponential decay, corresponding to constant probability of loss over time (Fig. 5*D*). The model also shows how different prion conformations, with potentially different elongation and fragmentation rates, can lead to different stabilities.

Using this model, we predicted that cells with larger volumes would have lower partitioning errors, which would make the prion more stable (*SI Appendix*, Fig. S9 *E* and *F*). To test this prediction experimentally, we used a mutant with longer cell size but with the same growth rate [*ftsN* deleted of codons encoding
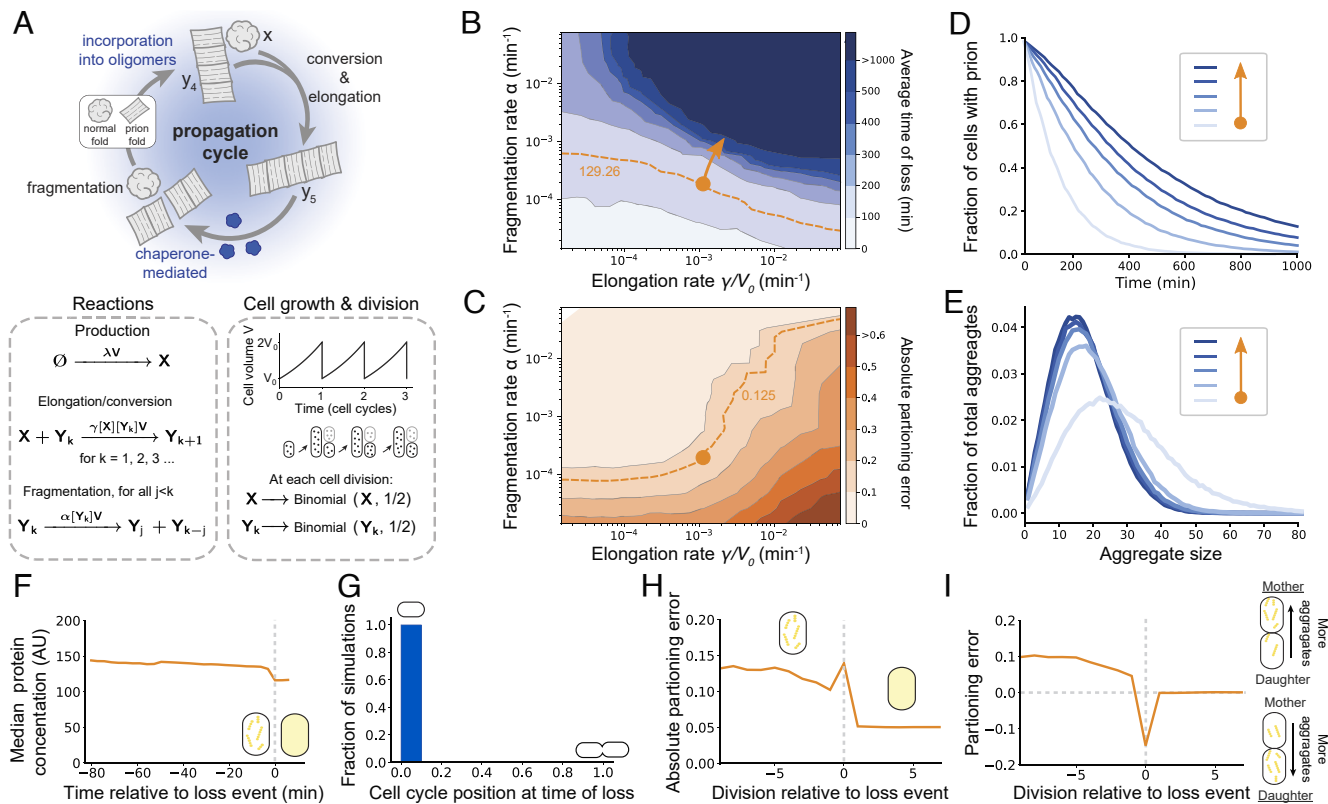
Fig. 5. A stochastic nucleated polymerization model recapitulates the experimental results. (*A*) A stochastic model of prion propagation in growing and dividing cells. Soluble fold protein numbers, denoted by X, are produced at a rate that scales with the cell volume. This phenomenological rate ensures that the concentration of soluble fold proteins is produced constitutively and reaches a cell-cycle independent state, in effect recapitulating the homeostasis of protein concentrations in exponentially growing cells (46) (*SI Appendix*, sections 3.2.1 and 3.2.8) . The number of prion fold aggregates made of k proteins is denoted by Y_k, where $k = 1, 2, 3, \ldots$. When a soluble fold protein collides with an aggregate of size k, it is converted with fixed probability to prion fold by elongating the aggregate to size $k + 1$. Assuming an equal distribution of aggregates in the cell volume, it follows (47) that the soluble fold proteins are converted to prion fold with a reaction rate proportional to the protein concentrations. Similarly, chaperone-mediated fragmentation follows a reaction that is proportional to the aggregate concentrations, with each binding between any two monomers having the same probability of splitting. Concentrations are given by dividing the protein numbers by the cell volume, which grows exponentially from V_0 to $2V_0$ between divisions with a fixed doubling time. At cell division, protein numbers are split randomly, with each soluble protein and each aggregate having a 50% chance of remaining in the cell. (*B*) Soluble fold production parameter λV_0 was estimated to be 1.75 min^{-1} by comparing the measured partitioning error of cells after loss of prions with their respective simulations (*SI Appendix*, section 3.2.3.2). With no minimal seed size $n_c = 0$ (see *SI Appendix*, section 3.2.5 for $n_c = 2$), a parameter sweep of elongation and fragmentation parameters shows that prions in cells with larger fragmentation and elongation rates are more stable. An average time of loss of 129.26 min was measured in the experiment shown in Fig. 1*F*, with the corresponding contour indicated by the dashed orange line. (*C*) Cells with smaller fragmentation rates and larger elongation rates have larger partitioning errors prior to loss. An absolute partitioning error prior to loss of 0.125 was measured in the experiment shown in Fig. 2*E*, with the corresponding contour indicated by the dashed orange line. Using the two contour plots from *B* and *C*, we find the model parameters that match the measured time of loss and partitioning error, indicated by the orange dot. (*D*) Time of loss curves follow an exponential, in agreement with Fig. 1*F*. Plotted are the time of loss curves for systems with parameters along the solid orange line in *B*. Loss is defined as when $Y_k = 0$ for all k. (*E*) The model can predict the aggregate size distribution prior to loss, showing that smaller aggregates are more stable in this parameter regime. (*F*) The total protein concentration is approximately constant leading up to the loss, in agreement with Fig. 2*B*. (*G*) In this model the prion state is always lost at cell division. (*H*) Absolute partitioning errors are larger before the loss, in agreement with Fig. 2*E*. (*I*) A large negative partitioning error occurs at the time of loss, in agreement with Fig. 2*F*.

amino acid residues 244-319, (49), *SI Appendix*, Fig. S10 *A*, *B*, and *D*], which revealed that the percentage of mutant cells that lost the prion during colony growth as assayed by replating experiments was half that observed with wild-type cells (*SI Appendix*, Fig. S10*C*). We thus concluded that partitioning errors played an important role in the loss of the prion, that cell volume affects prion loss, and that the nucleated polymerization model was consistent with our experimental results.

The model results are robust to many factors, like the initial conditions of the cells (*SI Appendix*, section 3.2.4 and Fig. S22), fluctuations in soluble fold protein production (*SI Appendix*, section 3.2.8), and fluctuations in chaperone concentrations (*SI Appendix*, section 3.2.7). However, these factors are an important consideration when the stochastic model is applied to other prion domains. For instance, fluctuations in soluble fold protein production that occur on a time-scale much longer than the time-of-loss (> 24 h) lead to a nonexponential prion loss curve

(*SI Appendix*, Fig. S21), and large pulses of chaperones can change the stability outside our experimental regime (*SI Appendix*, Fig. S19).

Discussion

Here, we used microfluidics and fluorescence microscopy to track thousands of individual cells propagating prion aggregates. Notably, cells tracked for over 20 generations with the prion would have likely renewed almost every single protein in the cell (and thus the prion proteins many times), showcasing the self-propagating nature of the prion aggregates. For proteins that are not degraded, half of the proteins are renewed after one cell division. Thus, after 20 cell divisions, $1/2^{20}$ of the $\sim 2^{21}$ original proteins will not have been renewed, such that only a handful of the original proteins will remain (50, 51).

small aggregates   old pole aggregates
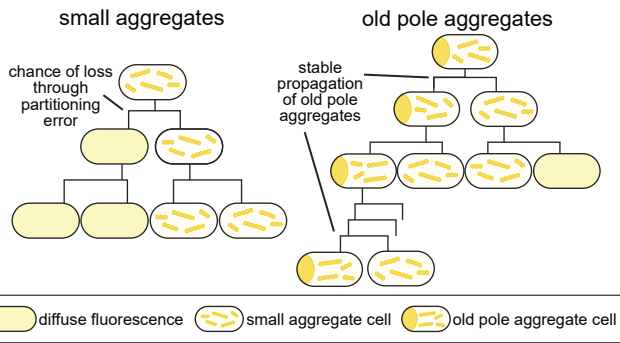
Fig. 6. Schematic of the two observed modes of prion propagation. Cells with small aggregates have a probability of losing the prion at each cell division through partitioning errors. At cell division, an old-pole aggregate cell generates a small aggregate cell and an old-pole aggregate cell. Although the old-pole aggregate is very stable, the cells containing old-pole aggregates represent a small fraction of a growing culture. The small aggregate cells generated through this division presumably propagate the prion similarly to the other observed small aggregate cells.

Modes of Propagation. We found that, for the three PrDs studied, the prions were propagated through two modes: stable old pole aggregates and less stable small aggregates (Fig. 6). We note that the old-pole aggregate cells also contain small aggregates. Therefore, at division, the old-pole cells generate one cell bearing an old-pole aggregate and one bearing small aggregates (Fig. 6). We have not investigated the formation of these old-pole aggregates, but speculate that they can be formed stochastically once an aggregate reaches a critical size. This critical size would prevent them from freely diffusing through the cell and confine them to the pole, while potentially also preventing chaperones from fragmenting them normally. It remains to be determined if other PrDs, from bacteria or other organisms, exhibit this type of propagation. We note that these cells would represent a small fraction of a growing culture (e.g., after 10 divisions, one old-pole cell would become 1 out of $2^{10} = 1,024$ cells), but could be observed in our microfluidic device as we are tracking the cells at the end of dead-end trenches. Yet, we conjecture that these old-pole aggregate cells could form a rare yet stable reservoir of the prion epigenetic state, generating cells containing small aggregates at each cell division. In fact, computational simulations suggest that the presence of this rare subpopulation of cells can increase the stability of the prion within the population as a whole (*SI Appendix,* section 3.2.10).

In contrast, the cells containing the small aggregates lost the prion relatively quickly, with a constant rate of loss over time (memoryless process with half-life of ~2 to 6 generations). We note that this stability will depend on the concentration of the prion protein, which was kept as low as possible during these experiments. The loss of the prion in these cells was driven mainly by a sudden mispartitioning of prion aggregates at cell division, resulting in a probability of losing the prion at each cell division (Fig. 6), consistent with the memoryless loss kinetics. It remains to be determined if other bacterial PrDs, such as the Rho PrD from *Clostridium botulinum* which had a lower rate of loss during replating (30), are propagated and lost similarly.

There is an interesting parallel between prion propagation and plasmid replication (52–54). As both rely on their own substrate for replication (i.e., autocatalytic replication), they must be partitioned to both cells at division to avoid extinction in the lineage. Plasmids impose a metabolic burden on their host but can provide fitness benefits under certain environmental conditions (e.g., antibiotic resistance). They have evolved regulatory mechanisms to control their copy number and to ensure partitioning to both cells (such as plasmid partitioning systems). Although prions are not associated with direct partitioning mechanisms, chaperones (e.g., Hsp104/ClpB) might be considered as conceptual analogues by breaking prion oligomers into smaller aggregates, thus facilitating the distribution of prion particles to daughter cells.

Different Lineages have Different Stabilities. In addition to disentangling the modes of propagation at the single-cell level, our microfluidic assay enabled precise quantification of the loss kinetics. This enabled us to observe that distinct lineages of the same PrD could propagate aggregates with distinct stabilities. In particular, we characterized one lineage of the *Ch* SSB prion that had a stability an order of magnitude greater than the others. This finding recapitulates and extends observations made in the previous study of the *Ch* SSB PrD, where both low-propagation and high-propagation lineages were characterized (31). These results are reminiscent of what has been observed in yeast, where one protein (e.g., Sup35) can form multiple self-propagating structures, called strains, with different stabilities (e.g., $[PSI^+]^{strong}$ vs. $[PSI^+]^{weak}$) (19, 55–58). Further work will be necessary to show whether the lineage-specific differences in stability observed in the case of the *Ch* SSB prion reflect different self-propagating structures.

Molecular Model of Prion Propagation and Challenges in Bacteria. Finally, we developed a stochastic implementation of the nucleated polymerization model that could recapitulate all the observed single-cell properties. In the future, the simple model could be tested further by perturbing the experimental parameters, e.g., by changing the concentration of the disaggregase ClpB (required for the propagation of the *Ch* SSB prion). This would indicate whether additional constraints that have been necessary to explain results in yeast, such as a size-dependent transmission of aggregates (45) or different seed sizes for prion strains (24), are also necessary. This model also reveals challenges for prion propagation in bacteria. Using the experimental measurements (partitioning errors and the average time of prion loss), we can estimate the total number of proteins, the fragmentation rate, and the elongation rate, and thus obtain an approximation for the replication rate ($\kappa = \sqrt{[monomer] \cdot \gamma\alpha}$, see *SI Appendix,* section 3.2.6). Even though the PrDs studied here appear to be lost relatively quickly, the estimated replication rate ($\sim 10^{-5}$/s) is of a similar order of magnitude to other prions, such as the mammalian PrP in vivo (23).

How does the model explain the discrepancy between the fast replication rate and the prion instability? *E. coli* is small and therefore has low numbers of proteins, which results in high partitioning errors. For example, the total number of proteins is ~100 times smaller in *E. coli* than in *S. cerevisiae*, which would result in partitioning errors ~10 times larger (i.e., $1/\sqrt{N}$). In addition, *E. coli* divides rapidly, which further reduces the stability of the prion, as proteins need to be converted to the prion state prior to the division for stable propagation. The lower stability we observed contrasts with what was observed in yeast, with, e.g., a loss rate of 10^{-5} generations^{-1} for $[PSI^+]$. Nevertheless, we speculate that lower stability does not necessarily make a prion less useful as an epigenetic switch. Prions have been suggested to provide an epigenetic state with fitness advantage under certain environmental conditions (4–6, 15, 16). The optimal stability of such an epigenetic state depends on the rate of

change of the environment experienced by the organism, which is difficult to estimate. Thus, whether a loss rate on the order of generations (for the PrDs studied here) or tens of thousands of generations (e.g., yeast [PSI^+]) is more or less useful biologically depends on temporal dynamics of the environment.

Materials and Methods

Detailed *Materials and Methods* are available in [SI Appendix](). The base strain used throughout the paper was *E. coli* MG1655. Prion formation was induced overnight by the production of the SSB PrDs fusion proteins and the New1 fusion protein with 10 μM IPTG at 30 °C. Cells were cured of the New1-containing plasmid by plating overnight at nonpermissive temperature (37 °C). These indicator plates contained X-Gal, which enabled distinguishing colonies with prion-containing cells (blue). For the microfluidic experiments, blue colonies were grown overnight at 30 °C, and the cultures were inspected with fluorescence microscopy to confirm that the cells contained prion aggregates. These confirmed cultures were then loaded into the microfluidic device, where the cells were continuously fed a supplemented M9 growth medium. Multiple cell positions were imaged in fluorescence every 8 min with a Zeiss Axio Observer at 63×, and the cell lineages were segmented and tracked as previously done (59).

Data, Materials, and Software Availability. The segmented and tracked lineage data are available on Zenodo (https://doi.org/10.5281/zenodo.8259944) (60), and the code for analyzing these data and generating the figures in the manuscript is available on GitHub (http://github.com/potvinlab/Jager2023_prion). The microscopy time-lapse images are available upon request due to their large size (they are several TB and logistically cannot be available online). The plasmids used in this study will be available on Addgene.

Author affiliations: [a]Department of Biology, Concordia University, Montréal, QC H4B 1R6, Canada; [b]Department of Microbiology, Harvard Medical School, Boston, MA 02115; [c]Department of Physics, University of Toronto, Toronto, ON M5S 1A7, Canada; [d]Department of Cell Biology, Harvard Medical School, Boston, MA 02115; [e]Department of Mathematics, University of Toronto, Toronto, ON M5S 2E4, Canada; [f]Department of Cell and Systems Biology, University of Toronto, Toronto, ON M5S 3G5, Canada; [g]Department of Physics, Concordia University, Montréal, QC H4B 1R6, Canada; and [h]Center for Applied Synthetic Biology, Concordia University, Montréal, QC H4B 1R6, Canada

1. S. B. Prusiner, Novel proteinaceous infectious particles cause scrapie. *Science* **216**, 136–144 (1982).
2. J. R. Glover *et al.*, Self-Seeded fibers formed by sup35, the protein determinant of [PSI^+], a heritable prion-like factor of *s. cerevisiae*. *Cell* **89**, 811–819 (1997).
3. H. L. True, S. L. Lindquist, A yeast prion provides a mechanism for genetic variation and phenotypic diversity. *Nature* **407**, 477–483 (2000).
4. C. M. Jakobson, D. F. Jarosz, Organizing biochemistry in space and time using prion-like self-assembly. *Curr. Opin. Syst. Biol.* **8**, 16–24 (2018).
5. S. A. Levkovich, S. Rencus-Lazar, E. Gazit, D. L. Bar-Yosef, Microbial prions: Dawn of a new era. *Trends Biochem. Sci.* **46**, 391–405 (2021).
6. M. F. Tuite, T. R. Serio, The prion hypothesis: From biological anomaly to basic regulatory mechanism. *Nat. Rev. Mol. Cell Biol.* **11**, 823–833 (2010).
7. A. Majumdar *et al.*, Critical role of amyloid-like oligomers of *Drosophila* Orb2 in the persistence of memory. *Cell* **148**, 515–529 (2012).
8. S. Chakrabortee *et al.*, Luminidependens (LD) is an *Arabidopsis* protein with prion behavior. *Proc. Natl. Acad. Sci. U.S.A.* **113**, 6065–6070 (2016).
9. L. Fioriti *et al.*, The persistence of Hippocampal-Based memory requires protein synthesis mediated by the prion-like protein CPEB3. *Neuron* **86**, 1433–1448 (2015).
10. F. Hou *et al.*, MAVS forms functional prion-like aggregates to activate and propagate antiviral innate immune response. *Cell* **146**, 448–461 (2011).
11. H. Xu *et al.*, Structural basis for the prion-like MAVS filaments in antiviral innate immunity. *eLife* **2014**, 1–25 (2014).
12. S. W. Liebman, Y. O. Chernoff, Prions in yeast. *Genetics* **191**, 1041–1072 (2012).
13. J. Li *et al.*, The RIP1/RIP3 necrosome forms a functional amyloid signaling complex required for programmed necrosis. *Cell* **150**, 339–350 (2012).
14. K. Si, Y. B. Choi, E. White-Grindley, A. Majumdar, E. R. Kandel, Aplysia CPEB can form prion-like multimers in sensory neurons that contribute to Long-Term facilitation. *Cell* **140**, 421–435 (2010).
15. G. A. Newby, J. S. Weissman, Blessings in disguise: Biological benefits of prion-like mechanisms. *Trends Cell Biol.* **23**, 251–259 (2013).
16. R. Halfmann *et al.*, Prions are a common mechanism for phenotypic inheritance in wild yeasts. *Nature* **482**, 363–368 (2012).
17. S. B. Prusiner, Molecular biology of prion diseases. *Science* **252**, 1515–1522 (1991).
18. L. Solforosi, M. Milani, N. Mancini, M. Clementi, R. Burioni, A closer look at prion strains: Characterization and important implications. *Prion* **7**, 99–108 (2013).
19. M. Tanaka, S. R. Collins, B. H. Toyama, J. S. Weissman, The physical basis of how prion conformations determine strain phenotypes. *Nature* **442**, 585–589 (2006).
20. B. H. Toyama, J. S. Weissman, Amyloid structure: Conformational diversity and consequences. *Annu. Rev. Biochem.* **80**, 557–585 (2011).
21. R. Krishnan, S. L. Lindquist, Structural insights into a yeast prion illuminate nucleation and strain diversity. *Nature* **435**, 765–772 (2005).
22. A. K. Itakura, A. K. Chakravarty, C. M. Jakobson, D. F. Jarosz, Widespread prion-based control of growth and differentiation strategies in *Saccharomyces cerevisiae*. *Molecular cell* **77**, 266–278 (2020).
23. G. Meisl *et al.*, Scaling analysis reveals the mechanism and rates of prion replication in vivo. *Nat. Struct. Mol. Biol.* **28**, 365–372 (2021).
24. J. Villali *et al.*, Nucleation seed size determines amyloid clearance and establishes a barrier to prion appearance in yeast. *Nat. Struct. Mol. Biol.* **27**, 540–549 (2020).
25. M. A. Nowak, D. C. Krakauer, A. Klug, R. M. May, Prion infection dynamics. *Integr. Biol.* **1**, 3–15 (1998).
26. S. S. Sindi, *Mathematical Modeling of Prion Disease. Prion-an overview* (InTech, 2017), pp. 207–227.
27. J. Masel, V. A. Jansen, M. A. Nowak, Quantifying the kinetic parameters of prion replication. *Biophys. Chem.* **77**, 139–152 (1999).
28. Y. Chernoff, S. Lindquist, B. Ono, S. Inge-Vechtomov, S. Liebman, Role of the chaperone protein Hsp104 in propagation of the yeast prion-like factor [psi^+]. *Science* **268**, 880–884 (1995).
29. V. Iglesias, N. S. De Groot, S. Ventura, Computational analysis of candidate prion-like proteins in bacteria and their role. *Front. Microbiol.* **6**, 1123 (2015).
30. A. H. Yuan, A. Hochschild, A bacterial global regulator forms a prion. *Science* **355**, 198–201 (2017).
31. E. Fleming, A. H. Yuan, D. M. Heller, A. Hochschild, A bacteria-based genetic assay detects prion formation. *Proc. Natl. Acad. Sci. U.S.A.* **116**, 4605–4610 (2019).
32. F. Gasset-Rosa *et al.*, Direct assessment in bacteria of prionoid propagation and phenotype selection by Hsp 70 chaperone. *Mol. Microbiol.* **91**, 1070–1087 (2014).
33. I. L. Derkatch, M. E. Bradley, J. Y. Hong, S. W. Liebman, Prions affect the appearance of other prions: The story of [PIN+] *Cell* **106**, 171–182 (2001).
34. I. L. Derkatch, M. E. Bradley, P. Zhou, Y. O. Chernoff, S. W. Liebman, Genetic and environmental factors affecting the de novo appearance of the [PSI^+] prion in *Saccharomyces cerevisiae Genetics* **147**, 507–519 (1997).
35. L. Z. Osherovich, J. S. Weissman, Multiple Gln/Asn-Rich prion domains confer susceptibility to induction of the yeast [PSI^+] prion *Cell* **106**, 183–194 (2001).
36. A. Yuan, S. Garrity, E. Nako, A. Hochschild, Prion propagation can occur in a prokaryote and requires the ClpB chaperone. *eLife* **10**, 02949 (2014).
37. P. Wang *et al.*, Robust growth of *Escherichia coli*. *Curr. Biol.* **20**, 1099–1103 (2010).
38. L. E. Greene, F. Saba, R. E. Silberman, X. Zhao, Mechanisms for curing yeast prions. *Int. J. Mol. Sci.* **21**, 6536 (2020).
39. D. Huh, J. Paulsson, Random partitioning of molecules at cell division. *Proc. Natl. Acad. Sci. U.S.A.* **108**, 15004–15009 (2011).
40. D. Huh, J. Paulsson, Non-genetic heterogeneity from stochastic partitioning at cell division. *Nat. Genet.* **43**, 95–100 (2011).
41. F. Ness, B. S. Cox, J. Wongwigkarn, W. R. Naeimi, M. F. Tuite, Over-expression of the molecular chaperone Hsp104 in *Saccharomyces cerevisiae* results in the malpartition of [PSI^+] propagons (2017).
42. M. E. Fernández-Tresguerres, S. Moreno-Díaz, F. de la Espina, R Giraldo Gasset-Rosa, A DNA-promoted amyloid proteinopathy in *Escherichia coli*. *Mol. Microbiol.* **77**, 1456–1469 (2010).
43. P. Lemarre, L. Pujo-Menjouet, S. S. Sindi, A unifying model for the propagation of prion proteins in yeast brings insight into the [PSI^+] prion (2020).
44. P. Lemarre, L. Pujo-Menjouet, S. S. Sindi, Generalizing a mathematical model of prion aggregation allows strain coexistence and co-stability by including a novel misfolded species. *J. Math. Biol.* **78**, 465–495 (2019).
45. A. Derdowski, S. S. Sindi, C. L. Klaips, S. DiSalvo, T. R. Serio, A size threshold limits prion transmission and establishes phenotypic diversity. *Science* **330**, 680–683 (2010).
46. J. Lin, A. Amir, Homeostasis of protein and mRNA concentrations in growing cells. *Nat. Commun.* **9**, 4496 (2018).
47. M. W. Covert, *Fundamentals of Systems Biology: From Synthetic Circuits to Whole-Cell Models* (CRC Press, 2017), pp. 114–121.
48. D. T. Gillespie, Exact stochastic simulation of coupled chemical reactions. *J. Phys. Chem.* **93555**, 2340–2361 (1977).

49. T. T. Truong, A. Vettiger, T. G. Bernhardt, Cell division is antagonized by the activity of peptidoglycan endopeptidases that promote cell elongation. *Mol. Microbiol.* **114**, 966–978 (2020).

50. R. Milo, What is the total number of protein molecules per cell volume? A call to rethink some published values *Bioessays* **35**, 1050–1055 (2013).

51. L. Arike *et al.*, Comparison and applications of label-free absolute proteome quantification methods on *Escherichia coli. J. Proteomics* **75**, 5437–5448 (2012).

52. G. Del Solar, M. Espinosa, Plasmid copy number control: An ever-growing story. *Mol. Microbiol.* **37**, 492–500 (2000).

53. J. Paulsson, M. Ehrenberg, Noise in a minimal regulatory network: Plasmid copy number control. *Q. Rev. Biophys.* **34**, 1–59 (2001).

54. J. Baxter, B. Funnell, Plasmid partition mechanisms. *Microbiol. Spectr.* **2**, 1–20 (2014).

55. I. L. Derkatch, Y. O. Chernoff, V. V. Kushnirov, S. G. Inge-Vechtomov, S. W. Liebman, Genesis and variability of [PSI] prion factors in *Saccharomyces cerevisiae. Genetics* **144**, 1375–1386 (1996).

56. S. M. Uptain, G. J. Sawicki, B. Caughey, S. Lindquist, Strains of [PSI^+] are distinguished by their efficiencies of prion-mediated conformational conversion *EMBO J.* **20**, 6236–6245 (2001).

57. B. H. Toyama, M. J. S. Kelly, J. D. Gross, J. S. Weissman, The structural basis of yeast prion strain variants. *Nature* **449**, 233–237 (2007).

58. M. R. Sawaya *et al.*, Atomic structures of amyloid cross-beta spines reveal varied steric zippers. *Nature* **447**, 453–457 (2007).

59. T. M. Norman, N. D. Lord, J. Paulsson, R. Losick, Memory and modularity in cell-fate decision making. *Nature* **503**, 481–486 (2013).

60. K. Jager *et al.*, Data for Measuring prion propagation in single bacteria elucidates mechanism of loss. Zenodo. https://doi.org/10.5281/zenodo.8259944. Deposited 17 August 2023.